PCCP

PAPER

View Article Online
View Journal | View Issue

Cite this: *Phys. Chem. Chem. Phys.*, 2025, **27**, 16435

Accelerated carbon dioxide mineralization and polymorphic control facilitated by nonthermal plasma bubbles

James Ho,[a] Matthew Hershey[b] and Dayne F. Swearer *[ab]

Mineralization of carbon dioxide is of interest for developing net-negative carbon technologies that mimic natural carbon cycles by removing and sequestering atmospheric carbon dioxide (CO_2). This study investigates plasma–liquid interactions (PLI) and the impact of modifying electron temperatures of nonthermal CO_2 plasmas to influence the nucleation and growth kinetics of calcium carbonate ($CaCO_3$). Through optimization of plasma discharge parameters, we show that plasma–liquid interactions can direct the formation of a pure vaterite phase of $CaCO_3$ over the more thermodynamically stable calcite phase under certain conditions. By varying the mole fraction of the discharge between a mixture of CO_2/Ar in the plasma bubbles, we show that increasing electron temperature enhances CO_2 capture, nucleation rate, and $CaCO_3$ yields. Increasing the electron temperature of the plasma by varying the Ar mole fraction in the flow increases CO_2 conversion nearly tenfold compared to pure CO_2 yet increases the competitive formation of carbon monoxide through CO_2 dissociation. When average electron energies were ~1 eV, the greatest selectivity toward $CaCO_3$ was observed. Our results support a mechanistic picture in which CO_2 mineralization is driven concurrently through gas-phase vibrational excitation of CO_2 and at the plasma–liquid interface by generating reactive hydroxyl species from plasma-activated water splitting. These plasma-generated species react to produce HCO_3^-, which is the rate-determining step in CO_2 mineralization. By demonstrating accelerated mineralization kinetics and polymorphic control of solid carbonate formation at plasma–liquid interfaces, this study could have broader relevance for engineering net-negative carbon sequestration technologies into solid forms for long-duration storage.

Received 27th March 2025,
Accepted 11th July 2025

DOI: 10.1039/d5cp01196e

rsc.li/pccp

1. Introduction

Mitigating anthropogenic climate change is one of the grand challenges facing modern society. With increasing human populations and expanded industrialization across the globe, research efforts to capture carbon and lock it into solid forms are becoming increasingly important for climate resilience. To reach a net-zero carbon target, society must reduce greenhouse gas emissions by 40–70% by 2050 compared to 2010 levels and reach net-neutral or net-negative carbon emissions by the end of the century.[1] A promising net-negative emission technology inspired by Earth's natural carbon cycle is the sequestration of CO_2 into carbonate minerals.[2,3] Carbonate minerals play a crucial role in marine sediments and impact ocean acidification by absorbing atmospheric CO_2 into calcium-enriched solutions.[4] Beyond their potential in CO_2 sequestration, carbonate minerals, such as $CaCO_3$, are widely used in applications

Dayne F. Swearer

Dayne Swearer is an assistant professor of Chemistry and Chemical & Biological Engineering at Northwestern University and is a faculty affiliate of the International Institute for Nanotechnology. Prof. Swearer received his PhD in 2019 from Rice University and completed postdoctoral training as an Arnold O. Beckman Postdoctoral Fellow in the Chemical Sciences at Stanford University. The Swearer Lab tackles interdisciplinary research questions spanning nanophotonics, heterogeneous catalysis, plasma chemistry, and various flavors of spectroscopy and microscopy. Prof. Swearer's early career achievements have been recognized through receipt of the 3M Non-tenured Faculty Award and the Packard Fellowship for Science and Engineering.

[a] *Department of Chemical and Biological Engineering, Northwestern University, Evanston, IL, USA. E-mail: dayne.swearer@northwestern.edu*
[b] *Department of Chemistry, Northwestern University, Evanston, IL, USA*

spanning construction,[5–7] biomedical engineering,[8,9] and gas storage.[10–12]

Lab-scale mineralization of $CaCO_3$ commonly involves bubbling $CO_{2(g)}$ into a supersaturated $Ca_{(aq)}^{2+}$ solution with a buffer such as ammonium hydroxide (NH_4OH) to facilitate $CO_{2(g)}$ absorption into the alkaline solution.[13–16] The rate of $CO_{2(g)}$ dissolution can be described as

$$r_{CO_2} = kC_B(C_{CO_2} - C_{CO_2,eq}) \quad (1)$$

where C_B is the concentration of $OH_{(aq)}^-$ ions in solution and k is the rate coefficient, which is dependent on the reaction temperature. The overall reaction proceeds as $Ca_{(aq)}^{2+} + 2Cl_{(aq)}^- + 2NH_4OH_{(aq)} + CO_{2(g)} \rightarrow CaCO_{3(s)} + 2Cl^- + 2NH_4^+{}_{(aq)} + H_2O_{(l)}$ and the individual reaction steps for this process can be written as follows:

$$\text{dissolution of } CO_2\text{: } CO_{2(g)} \rightarrow CO_{2(aq)} \quad (2)$$

$$\text{dissociation of } NH_4OH\text{: } 2NH_4OH_{(aq)} \rightleftharpoons 2NH_4^+{}_{(aq)} + 2OH_{(aq)}^- \quad (3)$$

$$\text{formation of } HCO_3^-\text{: } CO_{2(aq)} + OH_{(aq)}^- \rightleftharpoons HCO_3^-{}_{(aq)} \quad (4)$$

$$\text{formation of } CO_3^{2-}\text{: } HCO_3^-{}_{(aq)} + OH_{(aq)}^- \rightleftharpoons CO_3^{2-}{}_{(aq)} + H_2O_{(l)} \quad (5)$$

$$\text{nucleation of } CaCO_3\text{: } Ca_{(aq)}^{2+} + CO_3^{2-}{}_{(aq)} \rightleftharpoons CaCO_{3(s)} \quad (6)$$

where the formation of bicarbonate (4) is a rate-limiting step for $CaCO_3$ formation.[17] Numerous studies have explored pH ranges,[15,18,19] additives,[18–22] and temperature[23–25] for $CaCO_3$ growth in gas–liquid systems. Some have employed bubble reactors to demonstrate that the gas–liquid interface can significantly impact nucleation kinetics, particle formation, and the phase of the final $CaCO_3$ species.[13,14,26] In these mineralization processes, $CaCO_3$ precipitation is limited by mass transfer of $CO_{2(g)}$ into the solution and kinetic constraints resulting from $CaCO_3$ decomposition under increasingly acidic environments as a result of excess H_2CO_3 formation.[26]

Plasma–liquid interactions (PLI) are a promising platform to explore novel methods of particle synthesis and CO_2 activation by coupling the aqueous environment with an energetic plasma state to exploit unique chemical pathways and overcome these mass transfer limitations.[27–35] PLIs have been used for applications spanning nanomaterial synthesis,[32,36,37] organic synthesis,[37–39] wastewater treatment,[40,41] and biotechnology.[42,43] Nonthermal plasmas are characterized by electron temperatures greater than the temperature of heavier ionic and neutral species in the plasma, resulting in a deviation from the thermodynamic equilibrium. Like other states of matter, this plasma environment can interact with water, producing highly reactive radicals, UV photons, and free and solvated electrons.[27,30,43–46] Among these species, the $^{\bullet}OH$ radical is perhaps one of the most significant produced by plasma–liquid interactions in water due to its high oxidative potential and propensity to catalyse the generation of other reactive species (*e.g.*, H_2O_2), radical recombination, and other pathways.[44,47–49]

Plasma–liquid interactions can affect various solution properties, notably pH, through the generation of $OH_{(aq)}^-$ and $H_{(aq)}^+$, induce localized temperature increases due to electrical discharge, and alter solution conductivity.[50–52] Plasma-activated water can also modify the surface energies of particles

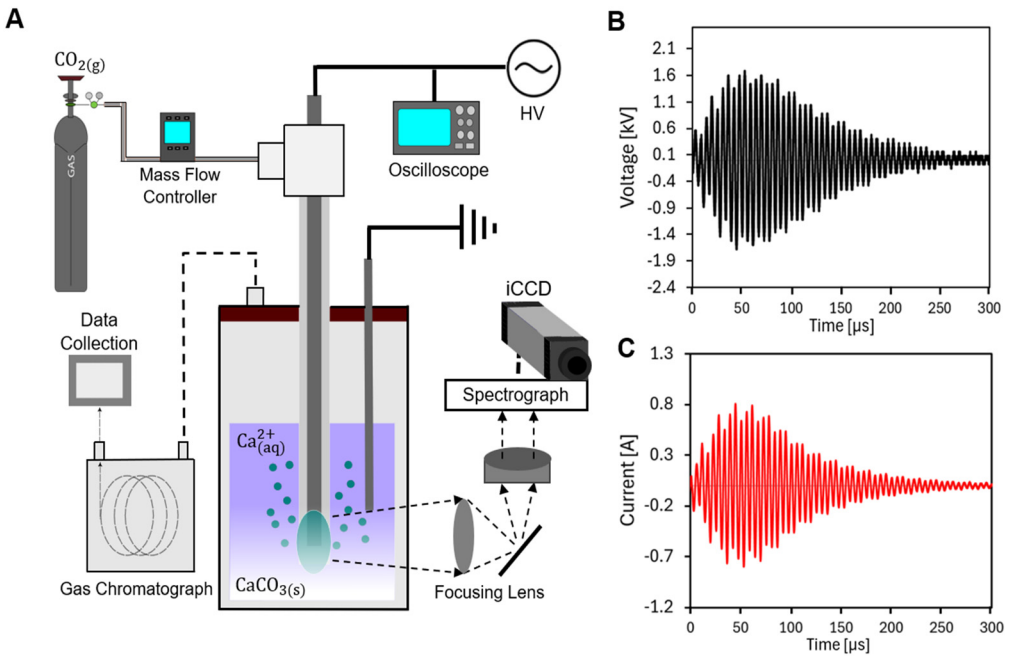

Fig. 1 Experimental overview and pulse plasma discharge characteristics. (A) An experimental schematic of the plasma bubble reactor for CO_2 mineralization to $CaCO_3$. (B) and (C) Example of nanosecond pulse voltage–current waveforms taken for the carbonation experiment where the frequency is 500 Hz, the duty cycle is 83 μs, and the resonance frequency is 60.00 kHz (CO_2 flow rate: 200 sccm). Solution conditions: 0.500 M $CaCl_2$ and 0.750 M NH_4OH in deionized (D.I.) water.

and promote sites for heterogeneous nucleation.[32] As a result, PLI can directly and indirectly influence particle growth and kinetics. The kinetics of PLI are complex and are affected by various solution properties—such as pH, concentration of reactive oxygen species, and conductivity of the solution—all of which depend on the plasma environment, making it challenging to gain mechanistic insights into particle growth.

This report demonstrates accelerated CO_2 mineralization *via* pulsed underwater electrical discharges within plasma bubbles (Fig. 1). This method has an advantage over discharging plasmas above the liquid surface, as plasma bubbles facilitate increased mass transfer between the gas and liquid phases and enhance the transport of reactive plasma intermediates in the aqueous environment through prolonged residence times, high internal pressures, and shockwave agitation from the bubble environment.[27,29,53] Here, we explored the effect of the plasma–liquid interfaces on the solution-phase chemistry of $CaCO_3$ precipitation. We show that factors such as plasma composition and discharge voltage influence the production of important plasma species, such as $OH_{(aq)}^-$ and vibrationally excited CO_2. These plasma-induced species directly impact the acid–base chemistry for $CaCO_3$ precipitation and enable control over $CaCO_3$ polymorph growth. Given the important role that net-negative carbon capture and utilization technologies must play in reaching global sustainability goals, this report on the pulsed discharge plasma bubble method provides a straightforward approach to tuning reaction dynamics crucial for solution-phase CO_2 mineralization. Furthermore, this demonstration that tailoring the plasma discharge characteristics controls the polymorphic phase presents evidence for carbon capture and utilization optimized toward applications in bioengineering and construction.[54–58]

2. Results and discussion

$CaCO_3$ can crystallize into three phases of increasing thermodynamic stability depending on aqueous reaction conditions: vaterite < aragonite ≪ calcite.[15,18,23,59] The mechanism of calcite growth has been well-studied and can be summarized as three key steps.[60] First, amorphous calcium carbonate (ACC) growth occurs upon carbonation onset of a supersaturated Ca^{2+} solution. ACC then undergoes dissolution and reprecipitation into spherical vaterite, followed by Ostwald ripening of vaterite into thermodynamically stable aragonite and calcite particles under prolonged time scales (seconds to minutes) and elevated temperatures.[15,19,60]

2.1 Voltage influence on the $CaCO_3$ phase and morphology

We first studied $CaCO_3$ nucleation as a function of plasma discharge on the resultant $CaCO_{3(s)}$ polymorph phase. A plasma bubble reactor (Fig. 1A) was employed to discharge pure CO_2 plasma bubbles into a 50 mL saturated (0.500 M) $CaCl_{2(aq)}$ solution under a constant flow rate. Experiments were repeated with fresh volumes of $CaCl_{2(aq)}$ at increasing discharge voltages. Current and voltage waveforms were recorded with a Tektronix 2 Series Mixed Signal Oscilloscope (Fig. 1B and C). Plasma mineralization experiments ceased after 5 minutes of plasma exposure. All precipitated $CaCO_3$ was isolated by vacuum filtration and analysed *ex situ* using powder-X ray diffraction (pXRD; Fig. 2A). After each experiment, the final solution temperature and pH were measured, and the vaterite phase weight percent was determined using Rietveld refinements (Fig. 2B). Increasing the discharge voltage increased the final

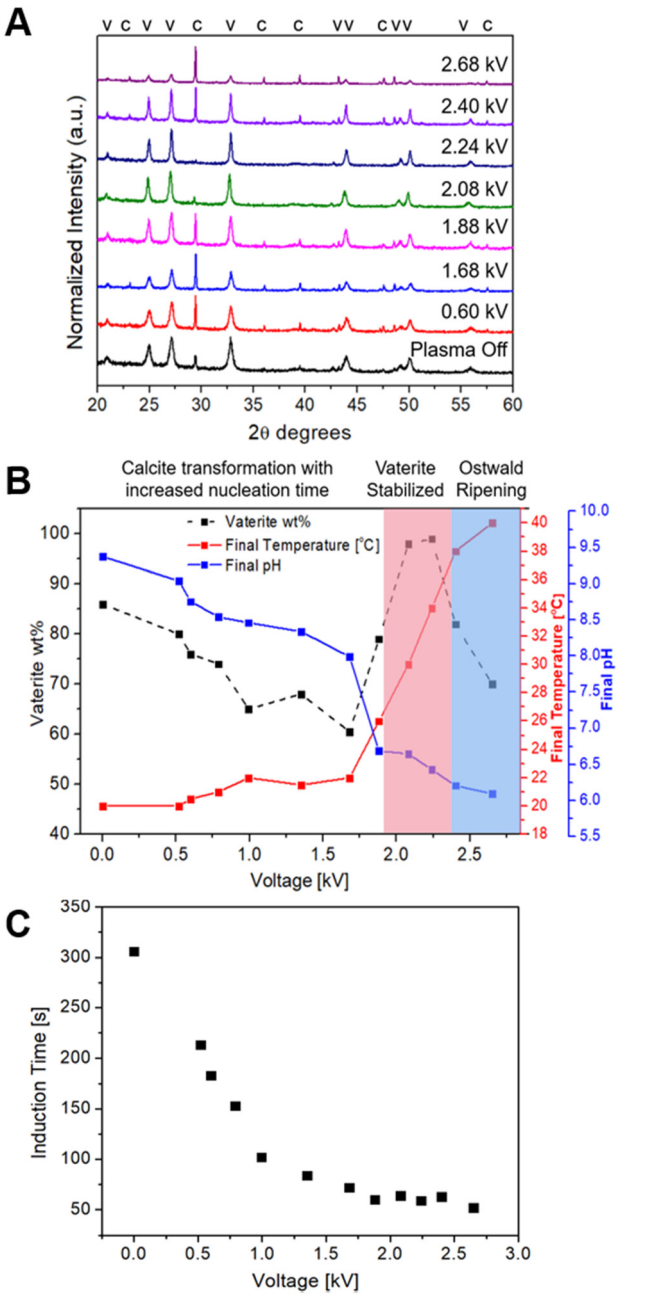

Fig. 2 (A) Powder X-ray diffraction of precipitated $CaCO_3$ at different plasma discharge voltages. (B) Discharge voltage-dependent formation of vaterite (wt%) and the final temperature and pH of the bulk solution after 5 minutes of plasma exposure. (C) Induction time at various applied plasma voltages. The induction times observed occur at pH values ranging from 10.00 to 9.50.

solution temperatures and decreased the final solution pH after 5 minutes (Fig. 2B). The increase in temperature was expected because of Joule heating resulting from the electric current. The pH at the beginning of each trial is kept constant at 11, and a decrease in pH over the course of plasma-assisted carbonation indicates the production of $HCO_3^-{}_{(aq)}$, suggesting that mineralization occurs more rapidly at plasma–liquid interfaces. This result is hypothesized to be an outcome of PLI where the $OH_{(aq)}^-$ species produced by water dissociation aid carbonation by increasing CO_2 dissolution and reacting with $OH_{(aq)}^-$ produced *in situ* to create $CO_3^{2-}{}_{(aq)}$ while in basic solution (reaction (5)). Given that an increase in pH was not observed, $OH_{(aq)}^-$ formation does not appreciably impact the reaction equilibrium in the presence of the buffer (reaction (3)).

From pXRD analysis, all reactions resulted in $CaCO_3$ in a mixture of calcite and vaterite phases (Fig. 2A). Applied discharge voltages up to 2.0 kV initially correspond to a decrease in vaterite wt%. With increasing voltages, a greater fraction of vaterite undergoes phase transformation to calcite within 5 minutes (Fig. 2B). This difference can be explained by an increase in voltage and an observed decrease in induction time (Fig. 2C), which allows for longer carbonation and aging times at lower pH values. Vaterite growth occurs faster, allowing for Ostwald ripening into the more thermodynamically stable calcite phase. This phase transformation will continue unless the solution conditions allow for the stabilization of the vaterite phase. Interestingly, between discharge voltages of 2.00 and 2.25 kV, pXRD analysis revealed $CaCO_3$ with 99% vaterite phase purity. This result can be explained by the pH and temperature of the reaction environment, which plays an important role in kinetically trapping metastable vaterite. In this region, a pH of 6–7 is optimal for producing high purity vaterite. However, across the $CaCO_3$ mineralization literature, the exact pH range favourable for vaterite formation remains disputed.[13,15,19,61,62] Temperature is also influential for vaterite stabilization, where elevated temperatures have been attributed to the transformation of thermodynamically stable calcite and aragonite. This has been reported to occur at temperatures above 30–35 °C,[62,63] which is consistent with the results herein with decreasing vaterite wt% at the highest voltage and temperatures. It is also important to note the role of NH_4OH in stabilizing vaterite in this process. Previous work has suggested that NH_4^+ and NH_3 may facilitate kinetic trapping and inhibit phase transition by buffering the pH of the solution favourable for vaterite stabilization.[15,64,65]

Precipitation begins once the supersaturation ratio, S, exceeds the solubility product, K_{sp}, of $CaCO_3$ and is influenced by the relative concentrations and activity of divalent ions, r (eqn (7)).

$$S = \sqrt{\frac{[Ca^{2+}][CO_3^{2-}]r^2}{K_{sp}}} \quad (7)$$

It is generally observed that at a low pH, $HCO_3^-{}_{(aq)}$ formation (reaction (4)) is most favoured in solution, whereas CO_3^{2-} formation (reaction (5)) is favoured at higher pH values.[15] Thus, decreasing pH results in a decrease in the supersaturation ratio and nucleation rate, J, according to the classical nucleation theory:[15,18–20]

$$J = A\exp\left[\frac{-16\pi\gamma^3\nu^2}{3(k_bT)^3}(\ln S)^{-2}\right] \quad (8)$$

In eqn (8), A is the pre-exponential factor, γ is the interfacial free energy between polymorphs, ν is the solid density, k_b is Boltzmann's constant, and T is the absolute temperature. This specific phase transformation proceeds *via* Ostwald's step rule of phases. At high supersaturation, the interfacial energy between polymorphs dominates, and metastable vaterite precipitates first, followed by more thermodynamically stable phases. As vaterite is thermodynamically unstable, it undergoes a phase transformation to calcite once these conditions are no longer favourable, *i.e.*, beyond a 2.25 kV discharge voltage of a pure CO_2 plasma. Extended times in solution will also favour the thermodynamic transformation of vaterite to calcite.

Scanning electron microscopy (SEM) was performed (Fig. 3) to track the morphology of calcite and vaterite. After 5 minutes of CO_2 bubbling without plasma (0 kV), $CaCO_3$ particles of primarily vaterite phase, characterized by uniform ellipsoidal particle morphologies, were precipitated. When plasma was introduced, the vaterite morphology was characterized mainly by spherical shapes, whereas calcite exhibited rhombohedral morphology. At 2.08 kV and 98% vaterite wt%, the morphology of $CaCO_3$ is primarily characterized by spherical/spheroidal vaterite with minor rhombohedral calcite. In contrast, at 2.24 kV with >99% vaterite, spherical vaterite dominated both in SEM and pXRD analyses. The ability to tailor nonthermal plasmas to produce vaterite-phase $CaCO_3$ selectively is particularly interesting, as this polymorph possesses enhanced porosity and solubility, along with distinct biochemical and optical

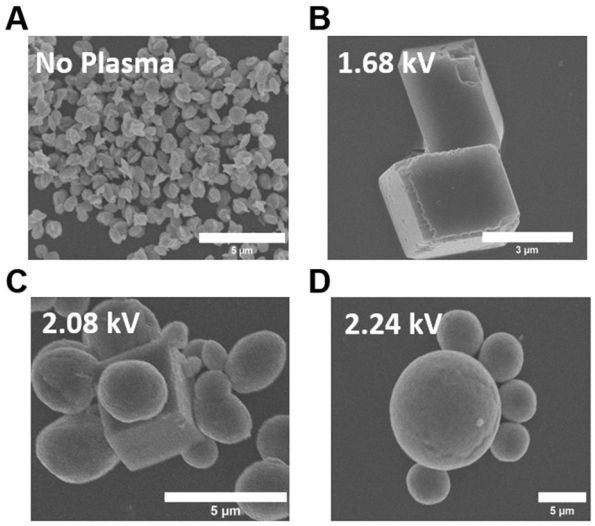

Fig. 3 Scanning electron micrographs of precipitated $CaCO_3$ at different discharge voltages showing the influence of phase purity on $CaCO_3$ morphology. (A) Ellipsoidal vaterite, (B) rhombohedral calcite, (C) spheroidal and rhombohedral vaterite and (D) spherical vaterite.

properties.[54–58] These properties make $CaCO_3$ in the vaterite phase the most practical for important biomedical applications such as bone grafting and drug delivery.[54–58]

2.2 The role of plasma-derived reactive species in nucleation

The rapid decrease in pH and resulting controlled nucleation of $CaCO_3$ polymorphs observed with CO_2 plasma bubbles at increasing discharge voltages motivated further investigation of how electron temperature affects nucleation and growth kinetics. The addition of argon (Ar) plasma into the CO_2 stream was investigated to understand the role of increasing electron temperature in nucleation. Under specific operating conditions, plasma discharge characteristics differ depending on the gas used due to their differences in electron energy distribution function (EEDF).[66] Although Ar has a larger first ionization energy, Ar has a smaller breakdown voltage than CO_2 because its electron energy is inefficiently distributed amongst rotational and vibrational degrees of freedom in CO_2 plasmas. In contrast, monatomic Ar is limited to excitations of translational degrees of freedom. The mean free path of Ar is also longer, such that electrons can accelerate under electric fields to larger collisional impact kinetic energies that ionize and sustain plasma discharges.[67] Thus, Ar will produce more plasma-activated species with a longer average lifetime than pure CO_2, resulting in increased concentrations of solvated electrons and $OH_{(aq)}^-$ at the plasma–liquid interface. Conversely, CO_2 plasmas can host unique reactive species at the PLI, such as HCO_2^-, HCOOH, CO_2^+, and $C_2O_4^{2-}$, which can activate other pathways for nucleation.[34,35,68–70]

To monitor the effect of the plasma environment on nucleation kinetics, the induction time, determined as the time between initial carbonation and the onset of the solution opaqueness, was monitored. A control experiment was first performed by bubbling pure Ar plasma into the saturated 0.500 M Ca^{2+} and 0.750 M NH_4OH solution. No precipitate was formed without a source of CO_2 after letting the reaction run for up to 1 hour. To isolate the contributions of specific plasma species produced at the PLI, we defined three sets of experiments performed using mixed-feed and co-feed CO_2 and Ar streams (Fig. 4A). For each experiment, flow rates of 100 standard cubic centimeters (sccm) per minute of CO_2 and Ar (totalling 200 sccm) were maintained to ensure similar bubble mass transport in the reactor. For the co-feed experiments, two bubble columns were placed in the reaction vessel where CO_2

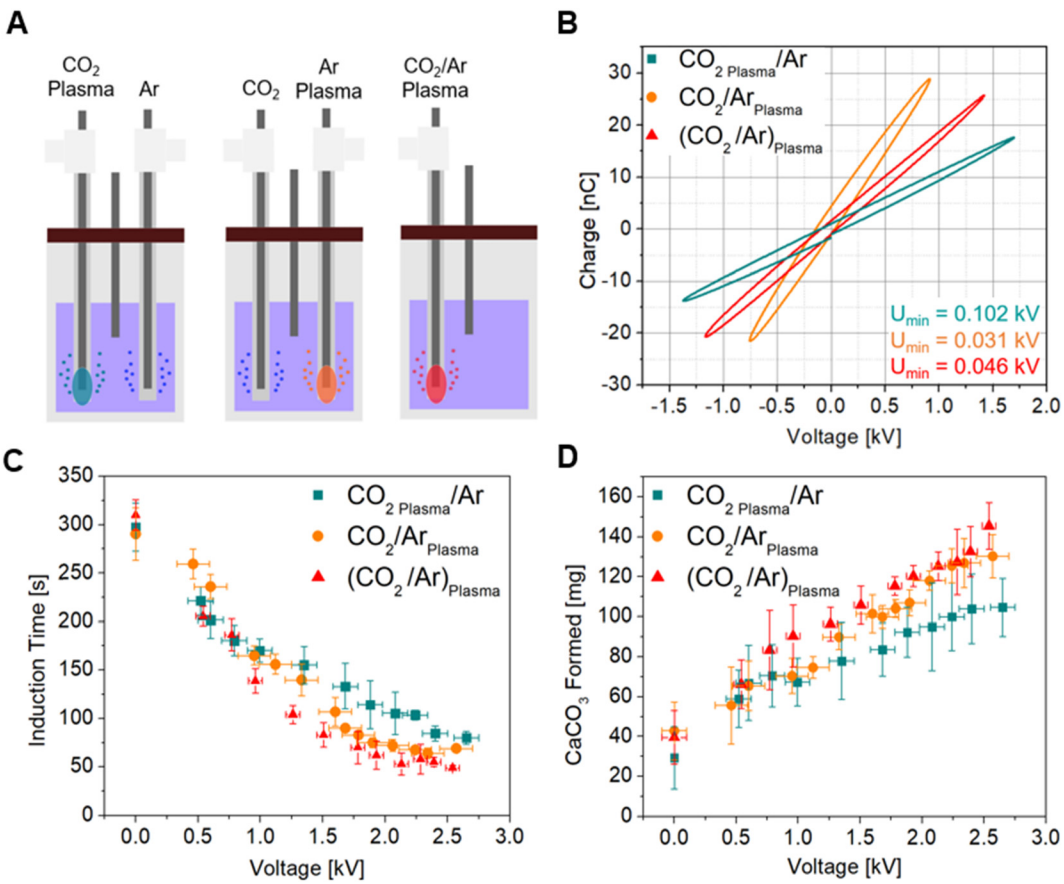

Fig. 4 (A) Experimental schematics of plasma-bubble mineralization reactor configurations with CO_2 and/or Ar plasmas. Left: CO_2 plasma and Ar (no plasma) bubbling separately. Middle: Ar plasma and CO_2 (no plasma) bubbling separately. Right: 50 : 50 CO_2/Ar plasma bubbling together. (B) Lissajous plots for each condition described in (A) where the plasma power is within 23–25 W. (C) Induction times for $CaCO_3$ nucleation as a function of discharge voltage in the plasma bubble reactor configurations are defined in (A). (D) Isolated yields of $CaCO_3$ as a function of plasma voltage. Precipitated $CaCO_3$ was collected after 5 minutes of plasma exposure.

and Ar flowed separately. We tested each bubble column separately with plasma on or off. In a third set of experiments, a single bubble column was used with mixed CO_2/Ar plasma at varying voltages. In all experiments, the discharge tube consisted of a closed-end quartz tube with eight 200 micrometer holes evenly spaced with constant total flow rates so that the bubble sizes were kept mostly constant. At a given applied voltage, the bulk solution temperature remained within less than 2.0 °C deviation for each reaction configuration. The plasma capacity for each system is studied through Q–U Lissajous analysis (Fig. 4B). The breakdown voltage of the plasma, U_B, is deduced from eqn (9):

$$U_B = U_{min} \times \frac{1}{1 + \frac{c_0}{c_p}} \quad (9)$$

where the plasma ''off'' capacitance, c_0, plasma ''on'' capacitance, c_p, and minimum voltage, U_{min}, are determined from fitting parameters from the Lissajous figure. The calculated breakdown voltage decreases with increasing Ar concentration (U_{B,CO_2} = 0.044 kV, $U_{B,CO_2/Ar}$ = 0.020 kV, and $U_{B,Ar}$ = 0.013 kV), which is expected given that Ar is easier to ionize than CO_2.

Induction occurs more rapidly in alkaline solutions where CO_2 can be absorbed and can react with $OH_{(aq)}^-$ to produce $HCO_3^-{}_{(aq)}$, which results in rapid pH decreases. The direct production of $OH_{(aq)}^-$ at the plasma–liquid interface is proposed to be the main cause of this observation, favouring $HCO_3^-{}_{(aq)}$ and lowering the pH to the point where the supersaturation begins to promote $CaCO_{3(s)}$ nucleation. This is observed by the decreasing pH and induction times (Fig. 2B and C) at increasing voltages. This also suggests that despite continuous production of $OH_{(aq)}^-$ at the local plasma–liquid interface, the bulk pH is governed by the competition of acidifying pathways in the reactor such as $CaCO_3$ mineralization. Across all voltage ranges studied, the condition where only CO_2 plasma bubbles were present with co-flow of Ar resulted in the slowest induction time (Fig. 4C). Mineralization with Ar plasma bubbles led to faster induction times, and experiments with mixed-feed CO_2/Ar plasma led to the quickest induction times. These trends of induction time as a function of voltage correlate to the isolated mass of precipitated $CaCO_{3(s)}$, where the equal volume of CO_2/Ar mixed-feed with plasma resulted in the greatest yield of $CaCO_{3(s)}$ (Fig. 4D). The increased nucleation rate of $CaCO_{3(s)}$ with experiments including a CO_2 plasma (Fig. 4D, teal and red markers) compared to when there is no plasma present (0.0 kV) is hypothesized to be due to increased activation of CO_2 to form $HCO_3^-{}_{(aq)}$ (reaction (4)). The faster induction time when Ar plasma was present is attributed to a greater presence of $OH_{(aq)}^-$ formed in solution from plasma-assisted water splitting,[48,71–73] which promotes the formation of $HCO_3^-{}_{(aq)}$ in accordance with Le Chatelier's Principle. As described above, Ar plasmas at the liquid interface generate more $^{\bullet}OH_{(aq)}$ and $OH_{(aq)}^-$ compared to pure CO_2 plasmas because of their greater average electron energies (see Fig. 5A and B). Under mixed-feed $(CO_2/Ar)_{Plasma}$, the reactivity of CO_2 is further enhanced through interaction with high-energy metastable Ar species under Penning ionization.[74,75] These contributions, in addition to the presence of more $OH_{(aq)}^-$ formed from greater average electron energies, are synergistic toward promoting $CO_{2(g)}$ dissolution and $HCO_3^-{}_{(aq)}$ formation. Under the most optimized conditions, mixed-feed $(CO_2/Ar)_{Plasma}$ is more energy efficient than co-flow CO_2/Ar_{Plasma} and $CO_{2Plasma}$/Ar experiments with energy consumption of 0.017, 0.024, and 0.027 kWh per g-$CaCO_3$, respectively. For the former, this enhanced energy utilization is a result of a higher mass yield of $CaCO_3$ and more efficient plasma ionization, as shown by Lissajous analysis.

It is important to note that an increase in average solution temperature is observed with increasing plasma voltages (20–40 °C). According to Henry's Law, $CO_{2(g)}$ solubility is expected to decrease with rising temperatures, resulting in a lower yield of $CaCO_{3(s)}$. Additionally, $CaCO_3$ formation is an exothermic process,[14] so according to Le Chatelier's Principle, such an increase in solution temperature should generally decrease the formation of $CaCO_3$. However, we found the reverse to be true. With increasing voltages, the mass of precipitated $CaCO_{3(s)}$ increased, suggesting that plasma activation of $CO_{2(g)}$ at liquid interfaces is crucial in accelerating mineralization and overcoming the thermodynamic limit of $CO_{2(aq)}$ in solution at elevated temperatures. We observed that the increasing yield of $CaCO_{3(s)}$ between experimental setups corresponds to those with a faster nucleation rate and that the greatest amount of precipitate formed resulted in the mixed-feed $(CO_2/Ar)_{Plasma}$ (Fig. 4D).

2.3 The role of electron temperature in reaction kinetics

Given that the mixture of CO_2 and Ar plasma best aided CO_2 mineralization to form precipitated $CaCO_{3(s)}$, we investigated the role of electron temperature at varying CO_2/Ar ratios. For these experiments, the output voltage was maintained at 2.0 kV, and the total flow rate was kept constant at 200 sccm. The electron Boltzmann equation solver, BOLSIG+, was used to calculate the electron temperature and simulate the EEDF at varying experimental CO_2/Ar fractions (Fig. 5A and B).[76] Simulations confirmed that the average electron temperature increased with decreasing CO_2 partial pressures. Average electron temperatures ranged between 0.95 eV and 3.19 eV at 100% and 10% CO_2 flows, respectively. These simulations were validated with optical emission spectroscopy (OES), which revealed Ca(II) H and K emission lines (393.4 nm and 396.9 nm, respectively) and Ca(I) emission at 422.7 nm that increased in relative intensity with increasing Ar fractions (Fig. 5C). As Ar has large ionization and excitation threshold energies (15.76 eV and 11.55 eV, respectively), inelastic collisions result in higher energy plasma electrons with longer average lifetimes, increasing the mean electron energy and relative intensity of the atomic Ca emission lines.[77] With increasing electron temperature, the $^{\bullet}OH_{(aq)}$ (308.9 nm, $A^2\Sigma \rightarrow B^2\Pi$) band intensity increased as well, indicative of increased rates of plasma-induced water dissociation.[27,73,78] The $^{\bullet}OH$ band is a key feature in describing the role of plasma–liquid interactions in accelerated mineralization, as it is a precursor to $OH_{(aq)}^-$ formation.[48,73] Subsequent increased

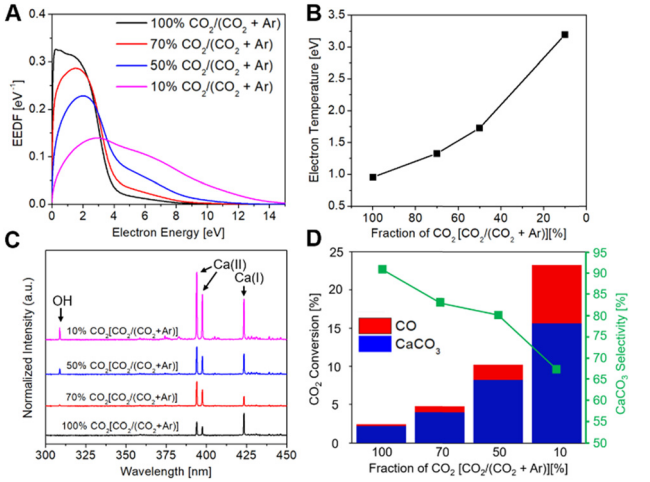

Fig. 5 (A) Simulated electron energy distribution functions and (B) simulated average electron temperatures under varying CO_2/Ar compositions. (C) Optical emission spectra (300–450 nm) of Ca and •OH spectral lines and (D) CO_2 conversion and $CaCO_3$ selectivity as a function of CO_2 mole fraction.

$OH_{(aq)}^-$ concentrations at the interface would shift the reaction equilibrium toward $HCO_{3\,(aq)}^-$ formation, the rate limiting step in mineralization.

In pure CO_2, a 2.5% conversion was measured, but it had the greatest selectivity for $CaCO_{3(s)}$. As the Ar fraction increased and, therefore, electron temperatures in the plasma increased, a decrease in the selectivity toward $CaCO_{3(s)}$ was observed with an increase in carbon monoxide (CO) formation as the sole measured carbon byproduct (Fig. 5D). With increasing Ar fractions, higher energy electrons can promote dissociation of CO_2 to form CO through direct electronic excitation–dissociation or step-wise vibrational ladder climbing.[68] Complementarily increased average electron temperatures also promoted plasma-activated water splitting to produce more •OH band, as confirmed using OES (Fig. 5C), shifting the equilibrium toward $CaCO_{3(s)}$ formation. In the experiments described here, the highest CO_2 conversion achieved was 23%, corresponding to a 10% CO_2 feed with balance Ar. Based on the ten-fold increase in CO_2 conversion from varying the argon composition from 0% to 90%, this result suggests that the electron energy distribution of the plasma has a profound effect on CO_2 mineralization at plasma–liquid interfaces.

The highest selectivity toward CO_2 mineralization over CO occurred in the systems with the lowest average electron energies. At the low (~1 eV) electron temperatures relevant here, plasma electrons mostly excite vibrational populations within the ground electronic state of CO_2, encompassing up to 97% total nonthermal discharge energy transfer of plasma electrons.[79,80] Although difficult to quantify, we propose that the vibrational excitation channel assists $CaCO_{3(s)}$ formation through the CO_2 bending mode. As CO_2 deviates from the idealized 180° bond angle, the electrophilicity of the central carbon atom increases and reduces activation barriers to nucleophilic addition of $OH_{(aq)}^-$. As more Ar is introduced into the feed, electron temperatures and Penning ionization increase, resulting in greater collisional energy transfer from metastable Ar exceeding that of ground state $CO_{2(g)}$, subsequently increasing the ratio of electron impact dissociation and electronic excitation–dissociation relative to the vibrational excitation pathway.[77,81] This hypothesis is theoretically and experimentally supported by the calculated average electron temperatures as a function of the CO_2/Ar ratio shown in Fig. 5B and product selectivity analysis displayed in Fig. 5D.

3. Conclusions

This work demonstrates that pulsed discharge plasma bubbles can accelerate CO_2 mineralization at aqueous interfaces and that plasma conditions can lead to the crystallization of specific $CaCO_3$ polymorphs, namely the spheroidal vaterite phase, over the more thermodynamically stable calcite phase. By simply changing the plasma voltage and composition, we show a four- to five-fold increase in $CaCO_3$ yield in 5 minutes compared to when no plasma is present. Although largely unoptimized, the best energy consumption reported from these trials is 0.017 kWh per g-$CaCO_3$. We propose a mechanism by which plasma-assisted CO_2 mineralization is driven concurrently through gas-phase vibrational excitation of CO_2 by low energy electrons (~1 eV) and at the plasma–liquid interface, where the generated reactive hydroxyl species from plasma-activated water splitting interacts at the bubble interface to produce HCO_3^-. To support this mechanism, we investigated the effect of the average electron temperature by varying the applied voltage in the gas discharge and diluting the feed with Ar. With Ar present, we observed an increase in the overall conversion of CO_2 from 2.5% to 23% through Penning ionization promotion. Still, the selectivity toward $CaCO_3$ decreased because of competing CO_2 dissociation to form CO, given higher average electron energies in the plasma and competition between electronic and vibrational excitation pathways. The greatest selectivity toward $CaCO_{3(s)}$ over CO was achieved by plasmas with lower average electron temperatures, which primarily excite vibrational populations in ground electron state CO_2. Beyond mineralization, this study lays the groundwork for exploiting plasma–liquid interfaces to electrochemically capture CO_2 for long duration storage whilst exploring how these parameters affect solution dynamics toward selective control over particle nucleation, phase, and morphology.

4. Experimental section

4.1 Plasma-assisted mineralization experimental setup

The plasma power supply (Leap100, PlasmaLeap Technologies) used in this setup can deliver high voltage pulses of up to 80 kV (peak-to-peak) with a repetitive pulse frequency ranging from 100 to 3000 Hz and a maximum output power of 400 W. The high-voltage and low-voltage/grounding electrodes consisted of a 240 mm length 316 stainless-steel rod and a 180 mm tungsten rod, respectively. The diameter of the electrodes was 3 mm.

A stainless-steel rod electrode, connected to a high-voltage Leap100 source, was placed inside a hollow quartz tube. A ground electrode and thermometer were placed in the reaction solution. The plasma bubble reactors were constructed using quartz tubes with inner and outer diameters of 6.0 mm and 10.0 mm, respectively, and a length of 180 mm. These tubes were capped with quartz at one end and open on the other for gas delivery through PTFE compression fittings. The capped end possessed uniform laser-drilled holes (200 μm diameter) to generate the plasma bubbles, which served as the only source of mass transfer in the reaction.

For each trial, 4 mL of a 0.750 M NH_4OH (Sigma Aldrich, 28%) buffer solution was added to 50 mL of a saturated 0.500 M $CaCl_2$ (Sigma Aldrich, 99.97%) solution. Ultrapure water (Milli-Q IQ 7000) was sourced and maintained at $\geq$18.2 MΩ. The gas (ultra-high purity grade CO_2 and Ar sourced from Airgas) flow rate was kept at a total flow rate of 200 standard cubic centimeters per minute (sccm) using an electronic mass flow controller (Alicat MFC). Unless noted otherwise, the reaction time for all experiments was set to 5 minutes based on prior experiments to optimize the $CaCO_3$ yield and rate of formation. The output voltage varied between 0.0 and 2.6 kV, and a constant duty cycle of 83 μs and frequency of 500 Hz were maintained. Upon carbonation, the reaction was monitored to observe the induction time. Traditional methods of quantifying the induction time by measuring solution conductivity were not feasible for this system, as the high electric field generated in the plasma discharge artificially alters the solution conductivity. Instead, the induction time was recorded in triplicate by visual observation when the solution turned from transparent into initial signs of solution turbidness.

A solution pH of 11 was measured initially for all trials and re-measured at the induction time and at the end of the reaction post-filtration. The pH at the induction was consistently observed between 9.50 and 10.00. After each experiment, the white $CaCO_3$ precipitate was vacuum filtered and air-dried at 70 °C overnight before further characterization.

The mole fraction of $CO_{2(g)}$ and $CO_{(g)}$ at the reactor outlet was determined by calibration curves using a gas chromatograph (SRI MG #5) equipped with an FID detector and methanizer.

Total CO_2 conversion was calculated using the following equation:

$$\text{CO}_2\text{ conversion }(\%) = \frac{F_{\text{CO}_2\text{in}} - y_{\text{CO}_2\text{outlet}} F_{\text{outlet}}}{F_{\text{CO}_2\text{in}}} \times 100$$

where F is the flow rate (sccm) and y is the gas mole fraction of CO_2.

4.2 Plasma diagnostics

The voltage and current required for plasma generation are recorded using a portable Tektronix 2 Series Mixed Signal Oscilloscope (MSO) to produce current–voltage waveforms. The applied voltage was captured using a high-voltage probe (Tektronix P6025A), while the current was measured using a current probe. The overall plasma power (P) was calculated using the following equation:

$$P = f\int_0^t v(t)q(t)\mathrm{d}t$$

where f is the frequency, t is the reaction time, and v and q are the voltages and charge measured using the oscilloscope. The energy consumption in kWh per gram of $CaCO_3$ was calculated as:

$$\text{Energy consumption} = \frac{P \cdot t}{g_{\text{CaCO}_3}}$$

During plasma operation, optical emission spectra (OES) were collected to measure chemical speciation in the plasma discharges and reactive species in the gas phase plasma. All OES data were collected using a PIMAX 1024 × 1024 iCCD (Teledyne Instruments) connected to an Acton 2500i triple grating spectrograph. OES measurements were taken in the dark to mitigate interference from ambient room lighting using free-space optics with a focusing lens.

4.3 Material characterization

Room temperature powder X-ray diffraction (pXRD) was performed on a STOE StadiP X-ray diffractometer with pure CuKα1 radiation (λ = 1.54056 Å). The experimental pXRD patterns were compared to simulated spectra of $CaCO_3$ calcite and vaterite morphology from open-source CIF files. Phase analysis and wt% of polymorph were determined by performing Rietveld Refinements with the GSAS II Software. A JEOL JSM-7900FLV scanning electron micrograph (SEM) with 8 kV acceleration voltage was employed to characterize the morphology of the synthesized $CaCO_3$ particles. Before imaging, the particles were dropcast in ethanol (1 mg mL^{-1}) and treated with osmium plasma coating to mitigate charging in the microscope.

4.4 Simulations

The electron Boltzmann equation solver, BOLSIG+, was used to determine electron energy distribution functions and electron temperatures of the CO_2/Ar plasma systems. The gas temperature used was 298 K, with a constant plasma density of 10^{17} m^{-3}, ionization degree of 10^{-2} and reduced electric field of 50 Td. We included the effects of electron–electron collision and chose a temporal growth model to describe the impact of electron production. The Phelps databases were referenced to acquire appropriate collisional reaction cross-sections.

Author contributions

J. H. wrote the initial manuscript and performed all experiments. M. H. collected scanning electron micrographs of the carbonate particles. D. F. S. conceived the central research question, secured funding, and managed the project. The final draft of the manuscript was edited and approved by all co-authors.

Conflicts of interest

There are no conflicts to declare.

Data availability

The data supporting this article are included in the text.

Acknowledgements

This work made use of the IMSERC crystallography facility at Northwestern University, which has received support from the Soft and Hybrid Nanotechnology Experimental (SHyNE) Resource (NSF ECCS-2025633) and the EPIC facility of Northwestern University's NUANCE Center, which also received support from SHyNE, and Northwestern's MRSEC program (NSF DMR-2308691). J. H. and M. H. gratefully acknowledge support from the Ryan Fellowship and the International Institute for Nanotechnology at Northwestern University. D. F. S. acknowledges support from the David and Lucille Packard Foundation, Breakthrough Energy Foundation, start-up funds from Northwestern University, and seed funding from the International Institute of Nanotechnology and Trienen's Institute for Sustainability and Energy. The U.S. Department of Energy, Office of Science, Office of Fusion Energy Sciences supported part of this work under award number DE-SC0024540.

References

1 Engineering the Sequestration of Carbon, **https://nae.edu/300509/Engineering-the-Sequestration-of-Carbon**, (accessed 23 January 2025).
2 P.-C. Chiang and S.-Y. Pan, *Carbon Dioxide Mineralization and Utilization*, Springer, Singapore, 2017.
3 S.-Y. Pan, Y.-H. Chen, L.-S. Fan, H. Kim, X. Gao, T.-C. Ling, P.-C. Chiang, S.-L. Pei and G. Gu, CO_2 mineralization and utilization by alkaline solid wastes for potential carbon reduction, *Nat. Sustainable*, 2020, **3**, 399–405.
4 G. Gadikota, Carbon mineralization pathways for carbon capture, storage and utilization, *Commun. Chem.*, 2021, **4**, 1–5.
5 F. Jin, M. Zhao, M. Xu and L. Mo, Maximising the benefits of calcium carbonate in sustainable cements: opportunities and challenges associated with alkaline waste carbonation, *npj Mater. Sustainable*, 2024, **2**, 1–7.
6 L. J. McDonald, M. A. Carballo-Meilan, R. Chacartegui and W. Afzal, The physicochemical properties of Portland cement blended with calcium carbonate with different morphologies as a supplementary cementitious material, *J. Cleaner Prod.*, 2022, **338**, 130309.
7 X. Fu, A. Guerini, D. Zampini and A. F. Rotta Loria, Storing CO_2 while strengthening concrete by carbonating its cement in suspension, *Commun. Mater.*, 2024, **5**, 1–14.
8 V. Lauth, M. Maas and K. Rezwan, An evaluation of colloidal and crystalline properties of $CaCO_3$ nanoparticles for biological applications, *Mater. Sci. Eng., C*, 2017, **78**, 305–314.
9 D. B. Trushina, T. V. Bukreeva, M. V. Kovalchuk and M. N. Antipina, $CaCO_3$ vaterite microparticles for biomedical and personal care applications, *Mater. Sci. Eng., C*, 2014, **45**, 644–658.
10 M. Luo, G. Zhang, Y. Fang, L. Cao, Z. Guo, K. Wang and J. Li, Calcium carbonate crystallization process from the mineralization of calcium chloride waste, *Sep. Purif. Technol.*, 2023, **319**, 124066.
11 O. Oloye and A. P. O'Mullane, Electrochemical Capture and Storage of CO_2 as Calcium Carbonate, *ChemSusChem*, 2021, **14**, 1767–1775.
12 Frontiers|Calcium Carbonate Precipitation for CO_2 Storage and Utilization: A Review of the Carbonate Crystallization and Polymorphism, **https://www.frontiersin.org/journals/energy-research/articles/10.3389/fenrg.2017.00017/full**, (accessed 12 November 2024).
13 D. Konopacka-Łyskawa, B. Kościelska and M. Łapiński, Precipitation of Spherical Vaterite Particles via Carbonation Route in the Bubble Column and the Gas-Lift Reactor, *JOM*, 2019, **71**, 1041–1048.
14 C. J. Grimes, T. Hardcastle, M. S. Manga, T. Mahmud and D. W. York, Calcium Carbonate Particle Formation through Precipitation in a Stagnant Bubble and a Bubble Column Reactor, *Cryst. Growth Des.*, 2020, **20**, 5572–5582.
15 I. Udrea, C. Capat, E. A. Olaru, R. Isopescu, M. Mihai, C. D. Mateescu and C. Bradu, Vaterite Synthesis via Gas–Liquid Route under Controlled pH Conditions, *Ind. Eng. Chem. Res.*, 2012, **51**, 8185–8193.
16 J. Heuer, Y. Kraus, M. Vučak and A.-P. Zeng, Enhanced sequestration of carbon dioxide into calcium carbonate using pressure and a carbonic anhydrase from alkaliphilic Coleofasciculus chthonoplastes, *Eng. Life Sci.*, 2022, **22**, 178–191.
17 W. Dreybrodt, J. Lauckner, L. Zaihua, U. Svensson and D. Buhmann, The kinetics of the reaction $CO_2 + H_2O \rightarrow H^+ + HCO_3^-$ as one of the rate limiting steps for the dissolution of calcite in the system H_2O CO_2 $CaCO_3$, *Geochim. Cosmochim. Acta*, 1996, **60**, 3375–3381.
18 N. Spanos and P. G. Koutsoukos, Kinetics of Precipitation of Calcium Carbonate in Alkaline pH at Constant Supersaturation. Spontaneous and Seeded Growth, *J. Phys. Chem. B*, 1998, **102**, 6679–6684.
19 Y. Sheng Han, G. Hadiko, M. Fuji and M. Takahashi, Crystallization and transformation of vaterite at controlled pH, *J. Cryst. Growth*, 2006, **289**, 269–274.
20 F. Liendo, M. Arduino, F. A. Deorsola and S. Bensaid, Nucleation and growth kinetics of $CaCO_3$ crystals in the presence of foreign monovalent ions, *J. Cryst. Growth*, 2022, **578**, 126406.
21 P. D. Natsi, S. G. Rokidi and P. G. Koutsoukos, Precipitation of Calcium Carbonate ($CaCO_3$) in Water–Monoethylene Glycol Solutions, *Ind. Eng. Chem. Res.*, 2019, **58**, 4732–4743.
22 K. Song, J.-H. Bang, S.-C. Chae, J. Kim and S.-W. Lee, Phase and morphology of calcium carbonate precipitated by rapid mixing in the absence of additives, *RSC Adv.*, 2022, **12**, 19340–19349.

23 M.-A. Popescu, R. Isopescu, C. Matei, G. Fagarasan and V. Plesu, Thermal decomposition of calcium carbonate polymorphs precipitated in the presence of ammonia and alkylamines, *Adv. Powder Technol.*, 2014, **25**, 500–507.
24 Y. A. Criado, B. Arias and J. C. Abanades, Effect of the Carbonation Temperature on the CO_2 Carrying Capacity of CaO, *Ind. Eng. Chem. Res.*, 2018, **57**, 12595–12599.
25 N. K. Bui, R. Kurihara, M. Kanematsu, H. Hyodo, T. Noguchi and I. Maruyama, Effect of temperature on binding process of calcium carbonate concrete through aragonite crystals precipitation, *Composites, Part B*, 2024, **283**, 111625.
26 J.-H. Bang, Y. N. Jang, W. Kim, K. S. Song, C. W. Jeon, S. C. Chae, S.-W. Lee, S.-J. Park and M. G. Lee, Precipitation of calcium carbonate by carbon dioxide microbubbles, *Chem. Eng. J.*, 2011, **174**, 413–420.
27 P. J. Bruggeman, M. J. Kushner, B. R. Locke, J. G. E. Gardeniers, W. G. Graham, D. B. Graves, R. C. H. M. Hofman-Caris, D. Maric, J. P. Reid, E. Ceriani, D. F. Rivas, J. E. Foster, S. C. Garrick, Y. Gorbanev, S. Hamaguchi, F. Iza, H. Jablonowski, E. Klimova, J. Kolb, F. Krcma, P. Lukes, Z. Machala, I. Marinov, D. Mariotti, S. M. Thagard, D. Minakata, E. C. Neyts, J. Pawlat, Z. L. Petrovic, R. Pflieger, S. Reuter, D. C. Schram, S. Schröter, M. Shiraiwa, B. Tarabová, P. A. Tsai, J. R. R. Verlet, T. von Woedtke, K. R. Wilson, K. Yasui and G. Zvereva, Plasma–liquid interactions: a review and roadmap, *Plasma Sources Sci. Technol.*, 2016, **25**, 053002.
28 I. Adamovich, S. Agarwal, E. Ahedo, L. L. Alves, S. Baalrud, N. Babaeva, A. Bogaerts, A. Bourdon, P. J. Bruggeman, C. Canal, E. H. Choi, S. Coulombe, Z. Donkó, D. B. Graves, S. Hamaguchi, D. Hegemann, M. Hori, H.-H. Kim, G. M. W. Kroesen, M. J. Kushner, A. Laricchiuta, X. Li, T. E. Magin, S. Mededovic Thagard, V. Miller, A. B. Murphy, G. S. Oehrlein, N. Puac, R. M. Sankaran, S. Samukawa, M. Shiratani, M. Šimek, N. Tarasenko, K. Terashima, E. Thomas Jr, J. Trieschmann, S. Tsikata, M. M. Turner, I. J. Van Der Walt, M. C. M. Van De Sanden and T. Von Woedtke, The 2022 Plasma Roadmap: low temperature plasma science and technology, *J. Phys. D: Appl. Phys.*, 2022, **55**, 373001.
29 B. S. Sommers and J. E. Foster, Plasma formation in underwater gas bubbles, *Plasma Sources Sci. Technol.*, 2014, **23**, 015020.
30 V.-P. Thai, H. Furuno, N. Saito, K. Takahashi, T. Sasaki and T. Kikuchi, The essential role of redox potential/equilibrium constant in the ability of non-equilibrium plasma for nanosynthesis in liquids, *J. Appl. Phys.*, 2020, **128**, 043305.
31 T. Merciris, F. Valensi and A. Hamdan, Synthesis of nickel and cobalt oxide nanoparticles by pulsed underwater spark discharges, *J. Appl. Phys.*, 2021, **129**, 063303.
32 U. R. Kortshagen, R. M. Sankaran, R. N. Pereira, S. L. Girshick, J. J. Wu and E. S. Aydil, Nonthermal Plasma Synthesis of Nanocrystals: Fundamental Principles, Materials, and Applications, *Chem. Rev.*, 2016, **116**, 11061–11127.
33 A. V. Nominé, Th Gries, C. Noel, A. Nominé, V. Milichko and T. Belmonte, Synthesis of nanomaterials by electrode erosion using discharges in liquids, *J. Appl. Phys.*, 2021, **130**, 151101.
34 T. Zhang, J. Knezevic, M. Zhu, J. Hong, R. Zhou, Q. Song, L. Ding, J. Sun, D. Liu, K. K. Ostrikov, R. Zhou and P. J. Cullen, Catalyst-Free Carbon Dioxide Conversion in Water Facilitated by Pulse Discharges, *J. Am. Chem. Soc.*, 2023, **145**, 28233–28239.
35 P. Rumbach, R. Xu and D. B. Go, Electrochemical Production of Oxalate and Formate from CO_2 by Solvated Electrons Produced Using an Atmospheric–Pressure Plasma, *J. Electrochem. Soc.*, 2016, **163**, F1157.
36 H.-T. Chen, D. Lee and S. Linic, Formation of Mixed Bimetallic Nanoparticles of Immiscible Metals through Plasma-Induced Reduction of Precursors in Solutions: A Case Study of Ag–Pt Alloy Nanoparticles, *Chem. Mater.*, 2023, **35**, 6557–6565.
37 J. Wang, N. B. Üner, S. E. Dubowsky, M. P. Confer, R. Bhargava, Y. Sun, Y. Zhou, R. M. Sankaran and J. S. Moore, Plasma Electrochemistry for Carbon–Carbon Bond Formation via Pinacol Coupling, *J. Am. Chem. Soc.*, 2023, **145**, 10470–10474.
38 D. Lee, H.-T. Chen and S. Linic, Plasma-Induced Selective Propylene Epoxidation Using Water as the Oxygen Source, *JACS Au*, 2023, **3**, 997–1003.
39 Y. Gorbanev, A. Nikiforov, I. Fedirchyk and A. Bogaerts, Organic reactions in plasma–liquid systems for environmental applications, *Plasma Processes Polym.*, 2025, **22**(1), e2400149.
40 M. Y. Naz, S. Shukrullah, S. U. Rehman, Y. Khan, A. A. Al-Arainy and R. Meer, Optical characterization of non-thermal plasma jet energy carriers for effective catalytic processing of industrial wastewaters, *Sci. Rep.*, 2021, **11**, 2896.
41 H. R. Khaledian, P. Zolfaghari, V. Elhami, M. Aghbolaghy, S. Khorram, A. Karimi and A. Khataee, Modification of Immobilized Titanium Dioxide Nanostructures by Argon Plasma for Photocatalytic Removal of Organic Dyes, *Molecules*, 2019, **24**, 383.
42 R. Zhou, R. Zhou, X. Zhang, J. Li, X. Wang, Q. Chen, S. Yang, Z. Chen, K. Bazaka and K. (Ken), Ostrikov, Synergistic Effect of Atmospheric-pressure Plasma and TiO_2 Photocatalysis on Inactivation of Escherichia coli Cells in Aqueous Media, *Sci. Rep.*, 2016, **6**, 39552.
43 R. Zhou, R. Zhou, P. Wang, Y. Xian, A. Mai-Prochnow, X. Lu, P. J. Cullen, K. (Ken) Ostrikov and K. Bazaka, Plasma-activated water: generation, origin of reactive species and biological applications, *J. Phys. D: Appl. Phys.*, 2020, **53**, 303001.
44 V.-P. Thai, T. N. Dam, K. Takahashi, T. Sasaki and T. Kikuchi, The generation pathways of OH and H_2O_2 by plasma-liquid interactions, *IOP Conf. Ser.: Earth Environ. Sci.*, 2023, **1278**, 012030.
45 C. D. Clay, C. M. Mueller, C. C. Rich, G. C. Schatz, P. J. Bruggeman and R. R. Frontiera, Evidence for Superoxide-Initiated Oxidation of Aniline in Water by Pulsed, Atmospheric Pressure Plasma, *J. Phys. Chem. Lett.*, 2024, **15**, 6918–6926.

46 D. C. Martin, D. T. Elg, H. E. Delgado, H. M. Nguyen, P. Rumbach, D. M. Bartels and D. B. Go, Optical and Chemical Measurements of Solvated Electrons Produced in Plasma Electrolysis with a Water Cathode, *Langmuir*, 2024, **40**(28), 14224–14232.
47 S. Keniley, N. B. Uner, E. Perez, R. M. Sankaran and D. Curreli, Multiphase modeling of the DC plasma–water interface: application to hydrogen peroxide generation with experimental validation, *Plasma Sources Sci. Technol.*, 2022, **31**, 075001.
48 F. Tampieri, M.-P. Ginebra and C. Canal, Quantification of Plasma-Produced Hydroxyl Radicals in Solution and their Dependence on the pH, *Anal. Chem.*, 2021, **93**, 3666–3670.
49 J. Liu, B. He, Q. Chen, J. Li, Q. Xiong, G. Yue, X. Zhang, S. Yang, H. Liu and Q. H. Liu, Direct synthesis of hydrogen peroxide from plasma-water interactions, *Sci. Rep.*, 2016, **6**, 38454.
50 X. Yang, C. Zhang, Q. Li and J.-H. Cheng, Physicochemical Properties of Plasma-Activated Water and Its Control Effects on the Quality of Strawberries, *Molecules*, 2023, **28**, 2677.
51 I.-E. Vlad and S. D. Anghel, Time stability of water activated by different on-liquid atmospheric pressure plasmas, *J. Electrost.*, 2017, **87**, 284–292.
52 R. Thirumdas, A. Kothakota, U. Annapure, K. Siliveru, R. Blundell, R. Gatt and V. P. Valdramidis, Plasma activated water (PAW): chemistry, physico-chemical properties, applications in food and agriculture, *Trends Food Sci. Technol.*, 2018, **77**, 21–31.
53 J. Hong, T. Zhang, R. Zhou, R. Zhou, K. (Ken) Ostikov, A. Rezaeimotlagh and P. J. Cullen, Plasma bubbles: a route to sustainable chemistry, *AAPPS Bull.*, 2021, **31**, 26.
54 D. Harpaz, H. Barhom, B. Veltman, P. Ginzburg and E. Eltzov, Biocompatibility characterization of vaterite with a bacterial whole-cell biosensor, *Colloids Surf., B*, 2023, **222**, 113104.
55 D. B. Trushina, T. V. Bukreeva, M. V. Kovalchuk and M. N. Antipina, $CaCO_3$ vaterite microparticles for biomedical and personal care applications, *Mater. Sci. Eng., C*, 2014, **45**, 644–658.
56 D. B. Trushina, T. N. Borodina, S. Belyakov and M. N. Antipina, Calcium carbonate vaterite particles for drug delivery: advances and challenges, *Mater. Today Adv.*, 2022, **14**, 100214.
57 L.-H. Fu, Y.-Y. Dong, M.-G. Ma, W. Yue, S.-L. Sun and R.-C. Sun, Why to synthesize vaterite polymorph of calcium carbonate on the cellulose matrix via sonochemistry process?, *Ultrason. Sonochem.*, 2013, **20**, 1188–1193.
58 L. Fan, F. Körte, A. Rudt, O. Jung, C. Burkhardt, M. Barbeck and X. Xiong, Encapsulated vaterite-calcite $CaCO_3$ particles loaded with Mg^{2+} and Cu^{2+} ions with sustained release promoting osteogenesis and angiogenesis, *Front. Bioeng. Biotechnol.*, 2022, **10**, 983988.
59 F. Liendo, M. Arduino, F. A. Deorsola and S. Bensaid, Factors controlling and influencing polymorphism, morphology and size of calcium carbonate synthesized through the carbonation route: a review, *Powder Technol.*, 2022, **398**, 117050.
60 P. Bots, L. G. Benning, J.-D. Rodriguez-Blanco, T. Roncal-Herrero and S. Shaw, Mechanistic Insights into the Crystallization of Amorphous Calcium Carbonate (ACC), *Cryst. Growth Des.*, 2012, **12**, 3806–3814.
61 P.-C. Chen, C. Y. Tai and K. C. Lee, Morphology and growth rate of calcium carbonate crystals in a gas–liquid–solid reactive crystallizer, *Chem. Eng. Sci.*, 1997, **52**, 4171–4177.
62 T. Ogino, T. Suzuki and K. Sawada, The formation and transformation mechanism of calcium carbonate in water, *Geochim. Cosmochim. Acta*, 1987, **51**, 2757–2767.
63 J. Chen and L. Xiang, Controllable synthesis of calcium carbonate polymorphs at different temperatures, *Powder Technol.*, 2009, **189**, 64–69.
64 J. M. Williams, D. Zhao, S. Moon, S. Kawashima, A.-H. A. Park and A. J. Moment, Stabilization of Pure Vaterite During Carbon Mineralization: Defining Critical Activities, Additive Concentrations, and Gas Flow Conditions for Carbon Utilization, *Cryst. Growth Des.*, 2023, **23**, 8103–8115.
65 X. Song, Y. Tuo, Y. Liang, Z. Tang, M. Li, X. Hua, R. Yang, X. Bu and X. Luo, Effects of NH + 4 concentration on the vaterite formation via direct carbonation use waste carbide slag under the different ammonium systems, *J. Environ. Chem. Eng.*, 2023, **11**, 111583.
66 J. Jonkers, M. van de Sande, A. Sola, A. Gamero and J. van der Mullen, On the differences between ionizing helium and argon plasmas at atmospheric pressure, *Plasma Sources Sci. Technol.*, 2002, **12**, 30.
67 M. A. Lindon and E. E. Scime, CO_2 dissociation using the Versatile atmospheric dielectric barrier discharge experiment (VADER), *Front. Phys.*, 2014, **2**, DOI: **10.3389/fphy.2014.00055**.
68 R. Snoeckx and A. Bogaerts, Plasma technology – a novel solution for CO_2 conversion?, *Chem. Soc. Rev.*, 2017, **46**, 5805–5863.
69 A. Mota-Lima, The Electrified Plasma/Liquid Interface as a Platform for Highly Efficient CO_2 Electroreduction to Oxalate, *J. Phys. Chem. C*, 2020, **124**, 10907–10915.
70 S. Yang, B. Zhao, I. A. Aravind, Y. Wang, B. Zhang, S. Weng, Z. Cai, R. Li, A. Z. Baygi, A. Smith, M. A. Gundersen and S. B. Cronin, CO_2 Reduction to Higher Hydrocarbons by Plasma Discharge in Carbonated Water, *ACS Energy Lett.*, 2021, **6**, 3924–3930.
71 M. Witzke, P. Rumbach, D. B. Go and R. M. Sankaran, Evidence for the electrolysis of water by atmospheric-pressure plasmas formed at the surface of aqueous solutions, *J. Phys. D: Appl. Phys.*, 2012, **45**, 442001.
72 G. Oinuma, G. Nayak, Y. Du and P. J. Bruggeman, Controlled plasma–droplet interactions: a quantitative study of OH transfer in plasma–liquid interaction, *Plasma Sources Sci. Technol.*, 2020, **29**, 095002.
73 Y. Yue, S. Exarhos, J. Nam, D. Lee, S. Linic and P. J. Bruggeman, Quantification of plasma produced OH and electron fluxes at the liquid anode and their role in plasma driven solution electrochemistry, *Plasma Sources Sci. Technol.*, 2022, **31**, 125008.
74 Ö. Şahin, İ. Tapan, E. N. Özmutlu and R. Veenhof, Penning transfer in argon-based gas mixtures, *J. Inst.*, 2010, **5**, P05002.

75 Z. Liu, F. Zhang, S. Wang, Y. Gao, B. Pang, X. Tantai and R. Zhou, Ar–CO_2 Mixture Plasma Jet Driven by Nanosecond Pulse at Atmospheric Pressure: Discharge Characteristics and Composition Analysis, *IEEE Trans. Plasma Sci.*, 2023, **51**, 2295–2301.
76 G. J. M. Hagelaar and L. C. Pitchford, Solving the Boltzmann equation to obtain electron transport coefficients and rate coefficients for fluid models, *Plasma Sources Sci. Technol.*, 2005, **14**, 722.
77 M. Ramakers, I. Michielsen, R. Aerts, V. Meynen and A. Bogaerts, Effect of Argon or Helium on the CO_2 Conversion in a Dielectric Barrier Discharge, *Plasma Processes Polym.*, 2015, **12**, 755–763.
78 P. J. Bruggeman, A. Bogaerts, J. M. Pouvesle, E. Robert and E. J. Szili, Plasma–liquid interactions, *J. Appl. Phys.*, 2021, **130**, 200401.
79 R. Aerts, T. Martens and A. Bogaerts, Influence of Vibrational States on CO_2 Splitting by Dielectric Barrier Discharges, *J. Phys. Chem. C*, 2012, **116**, 23257–23273.
80 A. Fridman, *Plasma Chemistry*, Cambridge University Press, Cambridge, 2008.
81 V. Goujard, J.-M. Tatibouët and C. Batiot-Dupeyrat, Carbon Dioxide Reforming of Methane Using a Dielectric Barrier Discharge Reactor: Effect of Helium Dilution and Kinetic Model, *Plasma Chem. Plasma Process.*, 2011, **31**, 315–325.

